

Manufacture of Soft-Hard Implants from Electrospun Filaments Embedded in 3D Printed Structures

Rand Alkaissy, Michael Richard, Hayley Morris, Sarah Snelling, Henry Pinchbeck, Andrew Carr, and Pierre-Alexis Mouthuy*

Rotator cuff tendon tears are common injuries of the musculoskeletal system that often require surgical repair. However, re-tearing following repair is a significant clinical problem, with a failure rate of up to 40%, notably at the transition from bone to tendon. The development of biphasic materials consisting of soft and hard components, which can mimic this interface, is therefore promising. Here, a simple manufacturing approach is proposed that combines electrospun filaments and 3D printing to achieve scaffolds made of a soft polydioxanone cuff embedded in a porous polycaprolactone block. The insertion area of the cuff is based on the supraspinatus tendon footprint and the size of the cuff is scaled up from 9 to 270 electrospun filaments to reach a clinically relevant strength of 227N on average. The biological evaluation shows that the biphasic scaffold components are noncytotoxic, and that tendon and bone cells can be grown on the cuff and block, respectively. Overall, these results indicate that combining electrospinning and 3D printing is a feasible and promising approach to create soft-to-hard biphasic scaffolds that can improve the outcomes of rotator cuff repair.

1. Introduction

In the musculoskeletal system one of the most common injuries are rotator cuff tendon tears (RCT) of the shoulder, contributing to 30–70% of all cases of shoulder pain.^[1] These tears are routinely surgically repaired by use of anchors which are fixed

into the humeral head. The torn tendon is then mechanically reattached with sutures emerging from the anchors. However, re-tearing following this repair is a significant clinical problem, with a failure rate of about 40%.^[2] These failures occur mostly at the transition from bone to tendon, i.e. the enthesis, which has an important role in the transmission of mechanical forces during motion.^[1,3–6] Other reported failure mechanisms of the repair construction are anchor pull-out, eyelet breakage, suture breakage, or tendon pulling through sutures (cheese-wiring).^[4,7,8] Conventional anchors are made of metal alloys or polymers, which can be biodegradable.^[9] Metallic screws provide good long-term fixation but also cause artefacts in postoperative imaging and complications including migration, whereas biodegradable materials provide short-term fixation but are associated with osteolysis and intraosseous cyst formation.^[10] Suture anchors have

consistently shown excellent mechanical properties^[11] but are not designed to biologically support native tissues to functionally repair.

Recent focus within the biomaterials field has aimed to produce implants that mimic the soft-hard tissue transition seen in the native enthesis.^[12,13] There has been an increasing interest in using electrospinning and 3D printing technologies to achieve this.^[14] Electrospinning is a process in which micro- and nanoscale fibers can be produced from a polymeric solution using electrical charges. These fibers have been shown to be architecturally similar in alignment and diameter to tendon collagen fibers and have resulted in positive contributions toward soft tissue repair.^[15] For hard tissue repair, 3D printing has shown promise because of its ability to produce structures with well-regulated architectural designs (e.g. porosity, pore size, and shape structure) that are easily reproducible.^[16] In terms of materials, polycaprolactone (PCL) and polydioxanone (PDO) have been extensively used with both technologies because of their appealing degradable properties, both polymers are degraded by hydrolysis and are metabolised in the body, and track record of safety in patients.^[17–20]

Combining electrospun (ES) and 3D printed (3DP) materials provides an exciting opportunity to engineer biomaterials for multiphasic tissues, such as the enthesis.^[21] So far, it has led to constructs for neuronal cell growth,^[22] bone tissue

R. Alkaissy, H. Morris, S. Snelling, A. Carr, P.-A. Mouthuy
Botnar Institute of Musculoskeletal Sciences
Nuffield Department of Orthopaedics
Rheumatology and Musculoskeletal Sciences
University of Oxford
Oxford UK

E-mail: pierre-alexis.mouthuy@ndorms.ox.ac.uk

M. Richard, H. Pinchbeck
3D LifePrints UK Ltd
Nuffield Orthopaedic Centre
Old Road, Oxford OX3 7LD, United Kingdom

 The ORCID identification number(s) for the author(s) of this article can be found under <https://doi.org/10.1002/mabi.202200156>

© 2022 The Authors. Macromolecular Bioscience published by Wiley-VCH GmbH. This is an open access article under the terms of the Creative Commons Attribution-NonCommercial-NoDerivs License, which permits use and distribution in any medium, provided the original work is properly cited, the use is non-commercial and no modifications or adaptations are made.

DOI: 10.1002/mabi.202200156

engineering,^[23] cartilage tissue engineering,^[24] and cranial defects.^[25] A variety of methods have been used which mostly involved 3D printing on top of pre-spun fibers or electrospinning on 3DP structures.^[26–28] However, none of these methods have been used to design soft-hard implants with a biphasic configuration that mimics the tendon–bone junction. This is mainly because the enthesis is particularly challenging to address as it is exposed to high forces, 152.6–779.2 N^[29–33], and high stresses, 11–22 MPa,^[29–31] while ES materials are typically relatively weak.^[34]

Here, we propose a new strategy to combine 3D printing and electrospinning and create robust soft-hard structures for potential as rotator cuff repair implants. Our strategy consists of embedding a soft cuff made of ES filaments during the 3D printing of a hard base. In this study, we investigate the use of PCL and PDO polymers and the effect of filament configuration on the mechanical properties of the cuff material. We also explore the impact of increasing the size of the cuff to reach clinically relevant mechanical strengths. Finally, we perform cell-based assays to assess the potential of the ES-3DP biphasic implant as a medical device.

2. Experimental Section

2.1. Preparation of Polymer Solution

PDO (Riverpoint Medical, USA) and PCL (Ashland Specialties Ireland, Laboratory A, Synergy Centre, Institute of Technology Tallaght, Ireland) granules were dissolved into 1,1,1,3,3,3-hexafluoroisopropanol (HFIP, Apollo Scientific Limited, UK) at concentrations of 7% and 17%, respectively (weight-to-volume ratios), based on optimization work performed previously.^[35,36] Small amount of pyridine (EMSURE ACS, Germany) was added to the PDO solution prior to spinning as described in previous work.^[35] The polymer solutions were put on a roller for at least 72 h at room temperature (RT) to ensure all granules were dissolved. Concentrations were selected based on optimization work previously carried out with the goal of creating submicron fibers that displayed no beading.^[15]

2.2. Electrospinning of Filaments

The filaments were produced from the polymer solutions as described previously.^[15] Briefly, electrospinning was performed with a single nozzle electrospinning setup and a wire collector (100 µm in diameter, Goodfellow, Huntingdon, UK) using a high voltage power supply system (30 kV, SL30P30/230, Spellman, West Sussex, UK) and a syringe pump (World Precision Instruments Limited, Florida, US). The metal wire was cleaned three times with 70% ethanol prior to use and was moving linearly at 0.5 mm s^{−1} during electrospinning. The solutions were spun with a voltage of 7.0–9.0 kV and were deposited onto the wire using a static nozzle. The material flow rate was 1 mL h^{−1}, spinning at a RT of 21 °C and 30% humidity. Following the exit of the metal wire (coated with the PCL material) from the glove box, the electrospun fibrous mesh was detached as a continuous filament and placed on a separate spool. The filament spool was removed at the end of the process and stored in a desiccator prior to stretching.

2.3. Preparation of Electrospun (ES) Filaments

After electrospinning, the filaments were manually stretched in a clean environment and at RT, at a ratio of about 1:3 and 1:7, respectively, for PDO and PCL. This was done to prevent plastic deformation during further use, as well as to increase the strength of the fibers, reduce the fiber diameter, and align the microfibers (see **Figure A1**, appendix A).^[15,17,37] The ends of the electrospun filaments were tied together whenever a break occurred to keep its continuity. They were wound on a spool and stored at room temperature in a desiccator before use.

2.4. Filament Assembly: Parallel and Twisted Configurations

The ES filaments were prepared in two configurations: parallel and twisted. For the parallel configuration, individual filaments were cut in 20 cm pieces, laid next to each other to ensure the fibers would not overlap or cross each other using tape. A minimum of 9 and a maximum of 27 parallel filaments were used in this study. They were then spanned onto aluminium U-frames which were created in-house (measuring 15 cm in length and width). The frames with the filaments were then stored in the desiccator until use.

For the twisted configuration, an industrial twisting machine (Mini Twister AMT 2S-Marui Textile Machinery Co. Ltd.) was used.^[36] Three spools of stretched filaments were loaded onto a feeder stand and twisted in the S-direction at a spindle speed of 500 turns min^{−1} to produce 3-ply yarns. Three spools of 3-ply yarns were then loaded onto the feeder again and twisted in the Z-direction at a spindle speed of 250 turns min^{−1} to produce a cabled yarn. These yarns were then also cut into 20 cm pieces and spanned across the frames using tape.

2.5. 3D Printing Parameters

The three-dimensional design of the block was created using computer-aided design (Autodesk Meshmixer, Autodesk Inc., San Rafael, CA, USA). The block dimensions were 5 × 15 × 10 mm (unless mentioned otherwise), with a lattice structure having an infill density of 60%. This denotes the amount of material that is printed within the overall object surrounded by an exterior wall. Samples were printed from PCL granules (Ashland Specialties, Ireland) with an Ultimaker 3 Extended 3D printer (3D4Makers, Haarlem, The Netherlands), operated by 3DLifePrints (Oxford, UK). The material was extruded at 110 °C and deposited in layers of 150 µm. No build plate heating was used in the PCL 3D printing process and all parts were printed at RT. A solvent free glue stick (chemical base: modified starch) was used to adhere the PCL print to the glass build plate of the 3D printer and prevent warping.

2.6. Incorporating the ES Filaments During 3D Printing to Create the Biphasic Constructs

An overview of the incorporation process of the ES filament into the 3D printed blocks is described in **Figure 1**. Following elec-

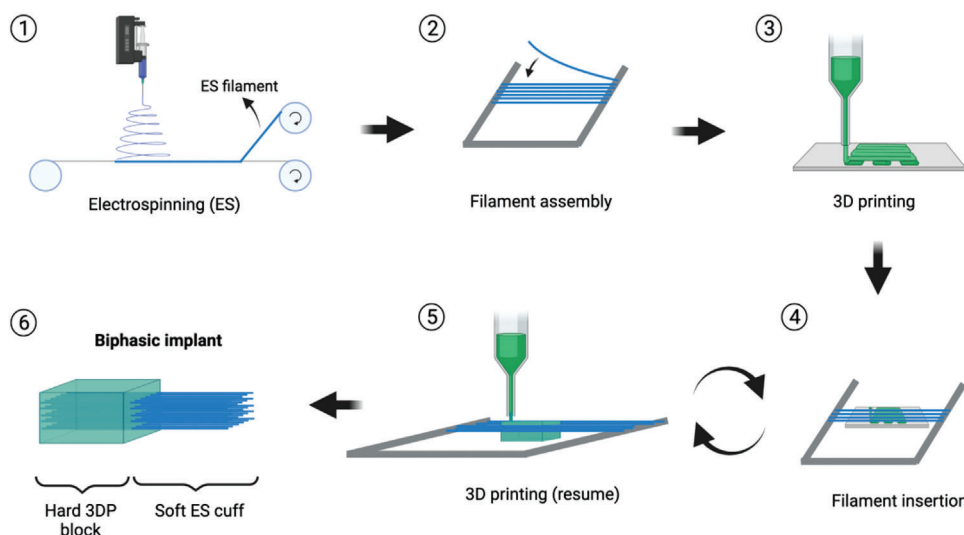


Figure 1. Schematic overview of the proposed approach to create soft-hard biphasic implant using electrospinning and 3D printing: 1) filament electrospinning, 2) assembly of the filaments onto U-frames, 3) initiation of the 3D printing, 4) interruption of the 3D printing to insert the electrospun (ES) filaments or yarns, 5) resuming of the 3D printing, 6) completed biphasic implant with an ES cuff and a 3D printed (3DP) block. Note that (4) and (5) are repeated as many times as needed.

Table 1. Interruption of the 3D printing based on the number of electrospun (ES) filaments layers. The minimum height of printed materials between layers was 0.45 mm and the final height of the blocks was 5 mm.

Number of layers of filaments in the print	Height at which the printing was interrupted [mm]
1	2.70
5	0.50, 1.40, 2.30, 3.20, 4.10
10	0.50, 0.95, 1.40, 1.85, 2.30, 2.75, 3.20, 3.65, 4.10

trospinning and assembly of the filaments onto the frames, 3D printing was initiated. The printing was automatically stopped to insert the ES filaments or yarns across according to the pre-defined number of layers (see Table 1). The pre-assembled fibers were quickly transferred from their U-frames and taped down on the printing platform to ensure that the movement of the nozzle would not disrupt their alignment. For the twisted yarns, the last 2 cm was untwisted and frayed so that each individual fiber would have maximum contact with the extruded material. Printing was then resumed, and the process was repeated until completion of the pre-defined number of steps to produce the biphasic construct, consisting of a soft cuff made of ES filaments or yarns and a hard 3D printed block.

2.7. Scanning Electron Microscopy (SEM)

Samples were cut and mounted on an aluminium stub (Agar Scientific, Essex, UK) with use of a carbon adhesive (Agar Scientific) and gold coated for 120 s with use of the SC7620 Mini Sputter Coater System (Quorum Technologies Ltd., UK). They were imaged by scanning electron microscopy (SEM; Carl Zeiss Evo LS15 Variable Pressure Scanning Electron Microscope) at various magnifications to examine the morphology of the samples. Measure-

ments were taken using ImageJ software (National Institutes of Health, Bethesda, USA).

2.8. Tensile Testing

Samples were tested to failure with a tensile testing machine (Zwick Roell Group, Ulm, Germany) using a 5 kN load cell and custom-made clamps that were previously described.^[38] During sample attachment to the grips, efforts were made to ensure that all filaments were under the same initial tension. The initial grip-to-grip separation was set at 10 cm and the test was then performed at a rate of 20 mm min⁻¹. The force at failure and change in distance between the grips were recorded with the testXpert II software (Zwick Roell Group, USA). The stress applied to the scaffold was calculated as $\sigma = F/A$ whereby F is the force (N) applied over the initial area A (mm²). An apparent cross-sectional area of 0.3 mm² and a porosity of 67% per filament were used to calculate the area of the filaments.^[38] The strain was defined as $\epsilon = (L_0 + L_i)/L_i$, whereby L_0 is the displacement value and L_i is the initial grip-to-grip distance. Six samples were tested per experimental condition to compare the different polymers and parallel and twisted configurations, whereas four samples were tested in the scale-up experiments.

2.9. Thermal Analysis

To assess the potential effect of the 3D printer nozzle's high temperature on the filaments during the printing process (in particular, at the exit of the printed block), PCL and PDO filaments were heated at different temperatures (60 °C, 80 °C, 90 °C, 100 °C, 110 °C, and 120 °C) in an oven (Fisherbrand Gravity Convection Oven) for 1 min. Fibers stored at RT were used as controls. A differential scanning calorimeter (TA Q2000-1275 Differential Scanning Calorimeter, DSC) was then used to evaluate the

thermal properties of the samples. For each condition, approximately 5 mg of sample was fitted in an aluminium pan (TZero Aluminium), along with an empty tin as the reference standard. The pans were heated a heating rate of 10 °C min⁻¹ in a nitrogen atmosphere, from 0 °C to 90 °C and -20 °C to 135 °C for PCL and PDO, respectively. A second heating and cooling cycle was performed to erase the thermal history of the sample and any residual solvent. From the differential scanning calorimetry (DSC) thermogram of the first cycle, the melting temperature (T_m), measured area of the thermal capacity (ΔH_m) and, if available, measured area of the annealing peak (ΔH_a) and of the recrystallization peak (ΔH_c) were determined.^[39] Recrystallization is observed as an exothermic peak just before the melting peak.^[40] Heat of fusion (ΔH_f) was calculated by averaging ΔH_m and considering the melting enthalpy of the recrystallization (ΔH_c) and of the annealing (ΔH_a) peaks, if observed ($H_f = (H_m - H_c) + H_a$).^[39,41] Crystallinity was calculated by dividing the resulting heat of fusion by the theoretical heat of fusion of a 100% crystalline sample (ΔH_f°) for PDO (141.2 J g⁻¹) and PCL (139.3 J g⁻¹), respectively.^[41,42]

$$\% \text{ crystallinity} = \frac{\Delta H_f}{\Delta H_f^\circ} \times 100\% \quad (1)$$

2.10. Cell Culture and Maintenance

For the soft ES cuff, human foreskin fibroblasts (HFF-1 cell line, ATCC) were maintained in growth medium DMEM F12 (Lonza, UK) supplemented with 15% foetal bovine serum (FBS, Biosera UK) and 1% penicillin-streptomycin solution (P/S, Gibco, UK), according to the supplier's instructions. For testing the hard 3DP blocks, a human osteoblast-like cell line was used (MG-63, Sigma Aldrich, UK). For the neutral red uptake assay, mouse BALB/c 3T3 fibroblast cells (Merck, Germany) were maintained at 37 °C, 5% CO₂ in Dulbecco's Modified Eagle Medium (DMEM, Sigma-Aldrich, UK) supplemented with 10% new-born calf serum (NCS, Sigma-Aldrich, UK), 4 × 10⁻³ M L-glutamine (Thermo Fisher Scientific, UK), 20 × 10⁻³ M 4-(2-hydroxyethyl)-1-piperazineethanesulfonic acid (HEPES, Thermo Fisher Scientific), and 1% penicillin/streptomycin (Gibco, UK). Cells were cultured in T-75 flasks (Thermo Fisher Scientific) with a fresh media change every 2 to 3 days. Once cells had reached approximately 90% confluency, they were split at a ratio of 1:3 and sub-cultured under the same conditions to allow proliferation with a maximum passage of 15 (BALB/c 3T3) and 20 (HFF-1 and MG-63). Cellular morphology and adherence was assessed prior to each media change and prior to cell seeding by light microscopy. In cases of unusual morphology and slow growth densities (i.e. round instead of flat and elongated cells) the flask was discarded. Culture medium was regularly tested for mycoplasma using a MycoAlert testing kit (Lonza, UK) according to the manufacturer's instructions.

2.11. Assessment of Cell Seeding and Attachment

Scaffolds ($n = 3$, biological repeats) were prepared for cell seeding by being soaked in culture media (DMEM F12 supplemented

with 15% FBS) and 1% P/S) for 2 h at 37 °C, 5% CO₂. Once cells had reached >90% confluency, they were mechanically scraped and counted using a hemacytometer counting-chamber device and seeded at different densities and volumes (Table 1). A standard curve was generated by seeding cells in triplicate ($n = 3$) at densities of 1 × 10⁴, 2.5 × 10⁴, 5.0 × 10⁴, and 1 × 10⁵ in a 48-well plate (Corning Inc., Corning, NY, USA). To estimate cell numbers from this curve a simple linear regression was applied using GraphPad Prism version 9 (GraphPad Software Inc, San Diego, USA). After seeding cells onto the scaffolds, the plate was placed in the incubator for 2 h to allow cells to attach (the seeding plate). Then, the scaffolds were transferred to a new 48-well plate and topped up with fresh culture medium. The seeding plate was saved to assess attachment of the cells on day 1. This was approximated by using a PrestoBlue assay (Invitrogen, Paisley, UK) to measure metabolic activity.^[43] This is an oxidation-reduction based assay in which resazurin, a blue nonfluorescent dye, is taken up by live cells and reduced to resorufin, a highly fluorescent component. This change in colour can be detected by measuring fluorescence in a microplate reader and obtaining a change in fluorescence intensity units (FIU) over time. It can therefore technically be used to quantify cellular proliferation and has the advantage of being nondestructive to cells so the same cell population can be evaluated across specified time points. Briefly, culture medium in each relevant well was replaced with 400 µL of a 10% PrestoBlue solution (v/v in DMEM) at selected time-points (days 1, 4, 7, 14 post-seeding) and incubated for 1 h at 37 °C, 5% CO₂. Afterwards, 100 µL of each sample was transferred in triplicate to a white, flat-bottom 96-well plate (Corning, UK). Fluorescence was measured at 485 nm excitation and 520 nm emission using a FLUOstar optima microplate reader (BMG Labtech, Germany). A well containing just the PrestoBlue solution was used to correct for background signal. The scaffolds were then rinsed with phosphate buffered saline (PBS) and transferred to new 48-well plates containing fresh, pre-warmed cell culture media. Scaffolds were placed into new 48-well plates with fresh medium every 2 to 3 days to exclude cells that had attached to the bottom of the well plates. The percentage of cells that had successfully attached to scaffolds was quantified by determining the ratio of the microplate readings (FIU) of the seeding plate and the scaffolds after day 1, corrected for background:

$$\% \text{ cell attachment} = \frac{\text{FIU day 1 plate}}{(\text{FIU day 1 plate} + \text{FIU seeding plate})} \times 100\% \quad (2)$$

The estimated cell number was then calculated using the calibration curve.

2.12. Assessment of Cytotoxicity

The NRU assay for cytotoxicity was used according to previously published work.^[36] It is an established method to indirectly evaluate toxicity in the biological evaluation of medical devices guided by the ISO 10993-5:2009.^[44] Prior to carrying out the assay, about 0.1 g of each sample (PDO ES filaments, PCL 3DP samples, Fiber-Wire sutures, polyethylene caps, rubber bands) was weighed out

and submerged in 70% ethanol for 2 h. They were then washed with sterile PBS (Sigma-Aldrich, UK) three times, transferred to separate 10-cm petri dishes, and left to dry overnight. The next day, samples were extracted at a ratio of 0.1 mg mL⁻¹ (guided by the extraction ratios outlined in ISO 10993-12 for irregularly shaped devices) in medium consisting of DMEM as described above but consisting of 5% NCS instead of 10%. The samples were incubated at 37 °C for 72 h under agitation. Next, BALB/3T3 cells were seeded into 96-well plates at a density of 1 × 10⁴ cells per well and left to adhere for 24 h to form a subconfluent monolayer. The different extraction media, corresponding to the testing materials, was added to the wells as undiluted, twofold and fourfold dilutions. The plate was incubated for another 24 h before neutral red uptake was determined and compared to control wells (cells exposed to DMEM only). Absorbance was measured at 540 nm using the FluoStar Optima microplate reader (BMG Labtech, Ortenberg, Germany). Cell viability was calculated as the percentage of values obtained for the cell culture medium only (control). Three technical repeats were used per experiment (*n* = 3). As recommended by the ISO 10993-12, sodium lauryl sulphate (SLS, Sigma-Aldrich, UK) was used as positive control and tested in a four-concentration scale.^[44] Rubber bands were used as a secondary positive control. Polyethylene caps were used as a negative control. Finally, FiberWire sutures (Arthrex, Naples, Florida, US) were used as a comparator to the PDO and PCL materials.

3. Statistical Analysis

Statistical analysis was performed with GraphPad Prism version 9 software (GraphPad Software Inc., California, USA). Data in graphs are expressed as means with standard deviations. A standard one-way ANOVA with Tukey's multiple comparisons testing was used to examine statistical differences between groups. Results were considered statistically significant for *p* < 0.05. Experiments were performed in six repeats for the mechanical testing, except for the scale-up manufacturing which was done in four repeats due to the amount of material it required. The thermal analysis was done in triplicate for both polymer types. Cytotoxicity was performed in triplicate.

4. Results and Discussion

4.1. Manufacturing Biphasic Scaffolds: PDO Soft Cuff versus PCL Soft Cuff

The novel approach described in the Experimental Section (Figure 1) was successfully applied to create soft-hard scaffolds consisting of a 3DP PCL block with an integrated ES cuff. As shown in Figure 2, the biphasic scaffolds could be produced with either a PDO or a PCL ES cuff; these prototypes were created with 60 filaments in total over four layers (15 filaments per layer). For the tensile tests shown in Figure 2I–L, the number of filaments per scaffold was downscaled to nine filaments per block for this initial stage. SEM images indicate that, while the PDO cuff morphology remained intact during the assembly, the microfibrillar morphology of the PCL cuff was lost near the insertion zone into

the 3DP block. This suggests that fibers melted as consequence of the melting point of PCL filaments (≈57 °C) being much lower than the temperature of the extrusion melt (≈110 °C) used during the 3D printing process (see Figure B1 and Table B1 in appendix B).

In terms of mechanical properties, biphasic scaffolds with a PDO cuff led to slightly higher breaking forces compared to the scaffolds with a PCL cuff (*p* = 0.0177, Figure 2I). However, controls performed with the ES cuff material only (no block) indicated that for both PDO and PCL, the insertion of the cuff in the block had a significant effect on its mechanical properties (*p* < 0.0001, Figure 2I). This is also evident from the respective stress and strain values (*p* < 0.0001, Figures 2J,K). A decrease in all properties was observed for the PCL cuff and this was expected because of the melting of the PCL filament near the insertion zone. For PDO, similar observations were made. While no melting was observed, this effect can be explained by annealing of the region of the filaments near the insertion. Annealing indeed occurs when PDO is exposed to high temperature.^[39] As shown in Table B1, a thermal analysis of the PDO filaments subjected to temperatures ranging from 60 °C to 120 °C for 1 min (to roughly mimic the contact with the extrusion melt before cooling down) indicated that the polymer crystallinity was affected by a short exposure at 90 °C and above (increase at 90 °C, decrease at 100–120 °C). This is shown in Figure B2 (appendix B). Annealing, and the subsequent change in crystallinity, have been linked to effect on the mechanical properties and degradation kinetics.^[39] The fact that all samples (PCL and PDO ES cuffs) failed at the interface between the soft and hard components (data not shown) is consistent with the explanations provided above. Further work, such as DSC analysis and SEM imaging of the failed regions, should however be carried out to confirm those failure mechanisms at the interface.

4.2. Cuff Design: Parallel Filaments versus Multifilament Yarns (PDO Cuff)

To investigate the effect of ES cuff design on the mechanical properties of the biphasic scaffolds, we compared twisted ES yarns to the parallel ES filaments previously presented (Figure 3A–D). This was done using the PDO filaments only, due to the melting of PCL filaments described in the previous section.

While possible, layering the twisted yarns was considerably more challenging than the parallel filaments because of the difficulty of maintaining alignment of the frayed ends and preventing individual filaments from crossing over each other and sticking together during printing due to the movement of the printer head. Therefore, the fabricated biphasic scaffolds with twisted yarns were of lesser quality and did not provide sufficient adhesion in the 3D printed layers. This was also evident when testing the scaffolds to failure, as they appeared to be slipping out of the blocks rather than breaking (as observed for the parallel filament configuration), indicating the smaller contact area between filaments and the 3D printed block, not sufficient to obtain proper adhesion. All samples failed just past the interface point and while the failure behavior differed, it is worth noting that—apart for the Young's modulus, which was slightly higher

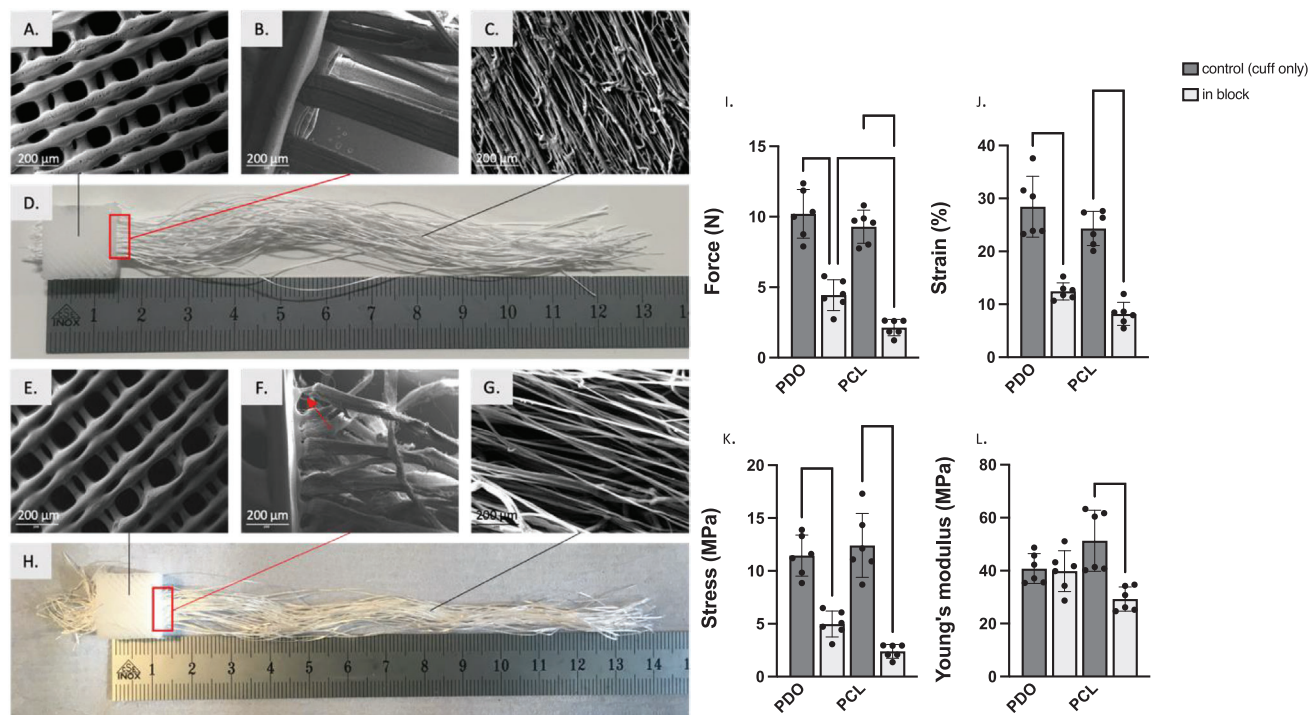


Figure 2. Soft-hard scaffolds made of a 3D printed (3DP) printed polycaprolactone (PCL) block and either a polydioxanone (PDO) (A–D) or a PCL (E–H) electrospun (ES) cuff. Scanning electron microscopy (SEM) images are taken of prototype scaffolds consisting of 60 filaments in four layers. A) SEM image showing the 3DP lattice (made of PCL) embedding the PDO cuff; B) SEM image showing the interface between the 3DP block and the PDO cuff; C) SEM image showing the submicron fibers within the PDO filaments; D) gross appearance of the biphasic scaffold with PDO cuff; E) SEM image showing the 3DP lattice (made of PCL) embedding the PCL cuff; F) SEM image showing the interface between the 3DP block and the PCL cuff; G) SEM image showing the submicron fibers within the PCL filaments; H) gross appearance of the biphasic scaffold with PCL cuff. I–L) Tensile properties of the biphasic scaffolds and control cuffs, each involving nine filaments in one layer: force at failure (I), maximum strain (J), maximum stress (K), Young's modulus (L), $n = 6$. Scale bars = 200 μm .

for twisted cuffs—the overall force, stress, and strain of biphasic implants did not change with the ES cuff design (Figure 3E–H). However, slippage of the twisted cuff means that those samples may have led to higher mechanical properties. Therefore, despite ES yarns being more challenging than parallel filaments to embed in the 3DP block, it could still be a strategy worth exploring in the future to create stronger structures.

Further work also needs to be done to propose better cuff designs such as by optimizing the number of twists within yarns. Indeed, the control cuffs (i.e. cuffs without a block), showed a negative effect of the twist on its mechanical properties: parallel cuffs were stronger than twisted yarns with an ultimate tensile strength of 10.2 ± 1.6 and 5.7 ± 1.7 N respectively ($p < 0.0001$, Figure 3E). This was unexpected as twisted yarns tend to perform better in terms of ultimate tensile strength due to the increased adhesions between filaments and thus higher frictional forces within the bundle.^[37] Such difference could be due to the degree of twisting being too high, resulting in (micro)fiber damage which potentially could have reduced the overall strength of the yarn.^[45] Furthermore, because the individual filaments within the yarn are not aligned to the axis in which load is applied, fiber obliquity can occur and this may also reduce the overall strength.^[46,47] Looking into these aspects were however out of the scope of this study and will be addressed in the future.

4.3. Scaling-Up the ES Cuff Size to Reach Clinically Relevant Forces

Figure 4 demonstrates the possibility to significantly increase the number of embedded filaments for the ES cuff to reach higher failure forces. Up to 27 ES filaments could be inserted across the width of the 3DP structure while 10 stops could be executed with the 3D printer, meaning that a maximum of 270 filaments could be embedded into the block. Figure 4A–C shows a single layer of 9, 18, and 27 filaments, respectively, and in Figure 4D–F the number of layers was increased to 5 to reach 90 filaments (5×18), and then to 10 to reach 180 filaments (10×18) and 270 filaments (10×27), respectively. A minimum of 0.45 mm of extruded material (corresponding to three passages of the printer head) was necessary between each layer of cuff material to ensure the lattice structure would not be compromised during printing. It was observed that reducing the layer height more than this would result in disruption of the lattice order. It is however worth noting that this is specific to the 3D printer that we have used. We anticipate that the minimum layer height could be further reduced with 3D printers offering better resolutions and future work should explore this. Smaller heights could indeed allow for more filaments to be inserted and this could increase the overall mechanical strength of the biphasic scaffold. Smaller layer heights may also reduce the vertical shear stress resulting from the gap between the cuff and

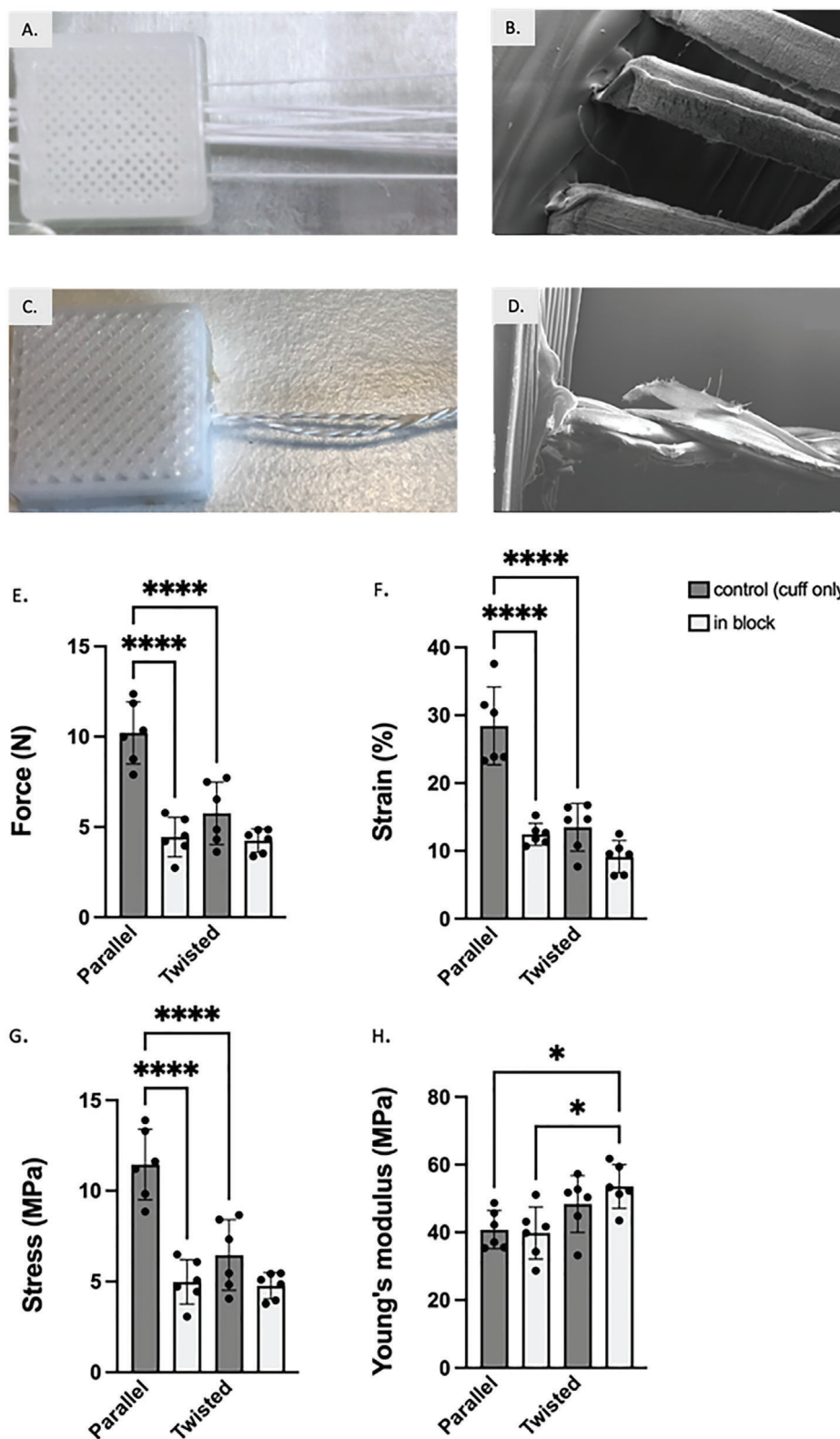


Figure 3. Electrospun (ES) 3D printed (3DP) biphasic scaffolds with ES filaments in a parallel or twisted configuration. A) Gross appearance of scaffolds with parallel filaments. B) Scanning electron microscopy (SEM) image showing nine parallel filaments in one layer emerging from the block. C) Gross appearance of scaffolds with twisted filaments. D) SEM image showing a twisted yarn (made of nine filaments) emerging from the block. E–H) Mechanical properties of the biphasic scaffolds and cuff controls, involving nine filaments in either twisted or parallel configuration. This included force at failure (E), maximum strain (F), maximum stress (G), Young's modulus (H) $n = 6$.

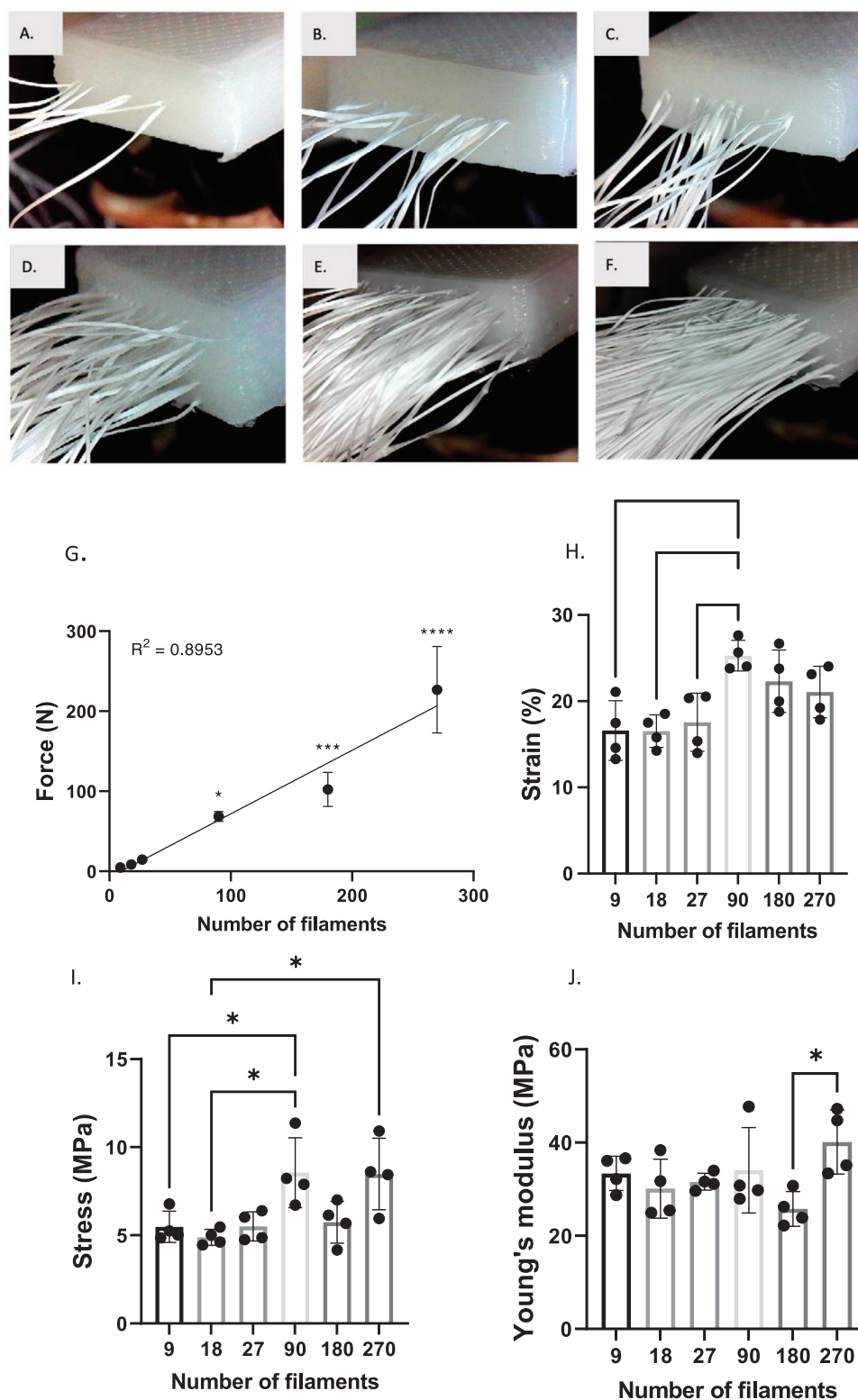


Figure 4. Increasing the cuff size to reach clinically relevant forces and demonstrate the scale up potential of the proposed approach. A–F) The number of filaments increased over the width (A–C) and height (D,E) with a maximum of 270 in 10 layers (F). Mechanical properties are portrayed (G–J) with force at failure (G), strain (H), stress (I) and Young's Modulus (J) per filament number, $n = 4$.

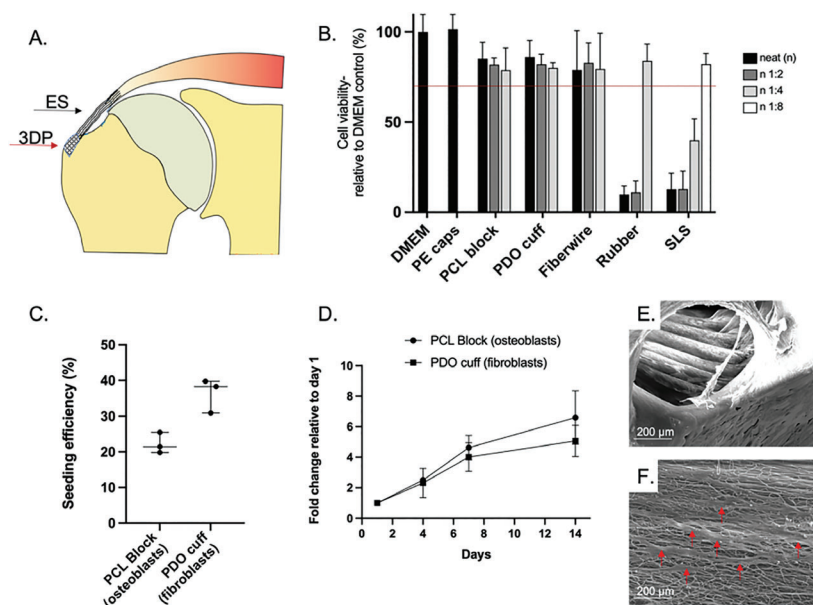


Figure 5. Cellular assays performed on the soft and hard components of the electrospun (ES) 3D printed (3DP) scaffold. A) Schematic of how the biphasic scaffold would fit into the shoulder joint, with arrows pointing to the individual components. B) NRU assay demonstrating the lack of cytotoxicity of the block and cuff component of the biphasic scaffold: cell viability was measured as a percentage of the vehicle medium (DMEM) and the materials were compared at undiluted concentrations (neat), 1:2 and 1:4 neat extract polyethylene (PE) caps were used as negative controls, rubber bands and sodium lauryl sulphate (SLS) served as positive controls and commercially available FiberWire sutures were used as a clinical material control). C) Cell seeding efficiency on the ES cuff and 3DP block fibroblast and osteoblasts cell lines, respectively. D) Relative cell growth on the materials over 14 days. E–F) Scanning electron microscopy (SEM) images showing cell morphology and spreading on the 3DP block and ES cuff (red arrows) at day 14, respectively. Scale bars = 200 μ m.

block phases (at the junction) and, as such, improve the overall mechanical properties of the scaffold. Furthermore, we did not explore alternative printing patterns or infill densities which can be used to modulate porosity and pore size, as this was out of the scope of this article. While porosity and pore size may affect the minimum layer height, they are also known to greatly influence cell attachment and infiltration in tissue engineering.

The force at failure of the scaled-up scaffolds exhibits a relatively linear relationship for the number of filaments inserted, as expected (Figure 4G). The maximum force of the scaffold including 270 filaments was 226.8 ± 46.9 N. The stress, strain, and Young's Modulus (Figures 4H–J) did not change with the increase in filaments, although a few significant differences were observed, e.g. stress and strain with 90 filaments. This was expected, since those properties are depending on the filament's inherent properties, not their number. The discrepancies observed for the cuff with 90 filaments were most likely due to batch effects as filaments may have been manufactured at different times. The calculated cross-sectional area did not take into account the spaces between inserted filaments which could have led to a variation in tension during tensile testing.^[48] Since every test involved the same materials with the same inherent properties, we expected the strain to remain consistent, irrespective of the number of filaments that was inserted. Finally, Young's Modulus (Figure 4J) was calculated as σ/ϵ and since both these values were similar across the range of scaffolds tested, it naturally follows that this produced a graph with little differences as well.

Figure 5A shows a schematic illustration of the concept of the biphasic scaffold inserted into the footprint area of the

supraspinatus tendon on the humeral head. The soft ES component would attach the tendon to the hard 3DP component embedded into the bone.

4.4. Biocompatibility of the Soft and Hard Components

To determine the cytotoxicity of the ES cuff (made of PDO) and 3DP block (made of PCL), an indirect NRU assay was performed. In this assay, guided by ISO 10993–5:2009, a relative cell viability above 70% indicates a noncytotoxic material. As shown in Figure 5B, a viability of 82.8% and 81.9% (relative to control culture medium) was observed in the neat extract for the cuff and block, respectively, confirming that both components are noncytotoxic. Positive controls (rubber and SLS) and negative controls (PE caps) were performed alongside the test samples to ensure that the assay was reliable. Furthermore, the compatibility of the ES cuff and 3DP block were compared to FiberWire, a well-known suture material used clinically in musculoskeletal tissue repair and no significant differences could be seen between those materials. These results were expected as both PDO and PCL have a clinical record of safety^[19,49] and are used at medical grade in this work. They confirm that the manufacturing methods, in particular the use of organic solvent during electrospinning, did not impact on the cytotoxicity of the implant. Solvent residuals can indeed be a source of toxicity^[50] and these results suggest that residual levels within the filaments were minimal.

The attachment, proliferation, and morphology of fibroblasts and osteoblast-like cells on the ES cuff and 3DP block,

respectively, are shown in Figure 5C,D. Fibroblasts were used to mimic behavior of tenocytes and osteoblast-like cells to mimic that of osteocytes. Seeding efficiency is 35% and 20% for the cuff and block, respectively (Figure 5C), similarly Savić et al. found a seeding efficiency of around 25% for their electrospun filaments and Salerno seeded to around 30–50% efficiency on 3D printed PCL scaffolds of varying porosities.^[36,51] This relatively low seeding efficiency may be explained by the highly hydrophobic nature of the material^[20] and the presence of large pores in the structure tested (gaps between filaments or in the 3DP lattice), which resulted in most of the cell suspension flowing down to the bottom of the well plate. Fibroblasts and osteoblasts proliferated similarly in terms of relative fold change on ES Cuff and 3DP respectively over 14 days (Figure 5D). Cells present on the materials are aligned along materials on the SEM images of Figures 5E,F. Cells on the ES cuff showed an elongated morphology (Figure 5F). These observations are consistent with the literature: primary cells seeded on electrospun filaments exhibit a fibroblast-like morphology by aligning themselves in the direction of the microfibers^[36,52] and while encouraging, future work is needed, using primary cells and co-culture models, to demonstrate cell migration within the materials and looking at their gene expression profile will be important to assess the healing potential of the biphasic scaffold.^[15,53–56]

5. General Discussion

This study aimed to create soft-hard biphasic scaffolds that could be used for enthesis repair by combining electrospinning and 3D printing. The presented approach can be used to produce biphasic implants that approach forces needed for clinical translation and is safe to use according to preliminary cell viability assays.

Efforts to recreate this interface in synthetic biomaterials have mainly focused on using chemical gradients, such as through increasing mineralization content with β -tricalcium phosphate or hydroxyapatite particles, and structural gradients, such as through progressive fiber alignments.^[57–62] Multiphasic or hierarchical scaffold strategies are particularly popular in the bone tissue engineering fields, but examples consist mostly of fiber-based scaffolds of differing diameters, and multilayered or multiphasic scaffolds condensed into a single unit.^[63–65] They do not reflect the two distinctly separate materials relating to the enthesis (bone and tendon) nor possess the mechanical properties required to support repair of the entheses of the shoulder joint. Furthermore, designs do not account for whether they would be able to fit into the desired implant location.^[66] For example, the native supraspinatus enthesis is incredibly small and therefore requires very concise scaffold dimensions to be able to fit an implant here. Since many orthopedic procedures are strictly arthroscopic this can pose a significant constraint as well.^[67] Another consideration is the biomechanics of the implant location, which can pose considerable geometric limitations.^[68] For example, an implant designed to fit into the supraspinatus area should be embedded completely level within the bone to prevent impingement happening when the shoulder abducts. Current suture and bone anchors are designed with this in mind.

Hybrid scaffolds made by electrospinning and 3D printing are currently being developed in the musculoskeletal field. Several strategies have been proposed, including: alternating between

electrospinning and 3DP printing^[23] electrospinning onto 3DP structures,^[27] printing on ES scaffold,^[25,69,70] assembling existing ES, and 3DP components.^[26,71] However, most of these strategies focus on bone applications and none attempted to recreate a soft-hard biphasic scaffold for application to entheses (e.g., at the rotator cuff).

Here, we demonstrate that ES-3DP scaffolds with a cuff made of up to 270 filaments can be created. The ES cuff was embedded into a region of 150 mm² (5 × 15 mm), an area that roughly reflects the dimensions of the footprint of the supraspinatus tendon enthesis, measured from human cadaveric specimens.^[72,73] The ES cuff had a maximum force of failure of 226.8 ± 46.9 N, indicating a clear potential for clinical application from a mechanical point of view. Indeed, sutures used for rotator cuff surgeries typically fail in the range of 184–359 N,^[11,74–76,77] although this is heavily dependent on suture material, suture configuration, and tissue quality (tendon and bone). In future work, however, reaching loads of 250 N might be beneficial as it has been suggested that such levels of strength are needed for early passive motion in postoperative rehabilitation.^[74,75] Data from human cadavers suggest that native supraspinatus tendon stresses and strain are between the ranges of 1.1–23 MPa^[29,31,33,78–80] and 1.4–28%,^[32,33,78,81] respectively. This broad range can be attributed to the different experimental setups and the quality of the specimens tested. However, the stress and strain values reported of the tested scaffolds in this work fall within this range. Very limited data exists on the Young's Modulus, but is in the range of ≈150 MPa for native supraspinatus tendon.^[33]

Several factors can be considered to further increase the maximum failure load of the ES cuff in the biphasic scaffold. Firstly, this could be done by improving the strength of the PDO filaments produced such as by decreasing the speed of the wire (to deposit more material) or increasing the concentration of pyridine in the polymer solution.^[35] Another factor to consider is textile design: although our attempt to use twisting to improve the ES cuff strength has been unsuccessful, assembly parameters were not explored in depth. Textile techniques such as braiding, twisting, weaving, and knitting have long been used in medical applications (e.g., sutures, grafts) to improve mechanical parameters and consequently have also been adopted in the fabrication of biomaterials.^[82–84] Thirdly, since the high temperature of the nozzle and extruded melt was identified as a potential issue leading to decreased strengths (through annealing), approaches that reduce the melt temperature or shield the filaments from heat during incorporation may lead to better results. Alternatively using an additive manufacturing process that does not involve melt deposition might be worth considering. Finally, modifying the print structure or working with a printer with better resolution might enable finer layers of material to be deposited and, as such, allow for the incorporation of more filaments and lead to higher strength values.

Overall, this study suggests that electrospinning and 3DP can be combined to produce biomaterials with robust soft-hard junctions that could help to regenerate entheses. However, it suffered from several limitations. Firstly, all scaffolds were fabricated by manually inserting filaments during the 3D printing process, leading to some variability between samples. Also, considering cost and time of manufacture of the scaffold components, the number of repeats for each sample was limited to either 4 or

6. Future work will benefit from more repeats while a more automated and efficient process will ensure more consistent scaffolds. Secondly, because of the large number of fibers required for building the biphasic scaffolds (e.g. 54 m per sample for those involving 270 filaments), filaments were often used from different batches and stored for prolonged periods of time (up to 3 months in desiccator). Batch-to-batch variations and degradation could account for differences observed in our mechanical datasets. Furthermore, while we performed mechanical test to failure, it would have been valuable to assess the scaffolds under cyclic loading regimes. It has been previously established that cyclic loads of between 100 and 180 N occur in supraspinatus tendon^[74,85,86] and material fatigue is a common failure mechanism among orthopedic implants. Fourthly, the design and materials used for the print and filament involved very little variations. There are many variations of the 3DP block or ES cuff that could be explored, in terms of structure, geometry, chemistry, etc. For instance, we only printed the base from PCL, which is a polymer well known for its clinical use, but which is highly hydrophobic and leads to relatively low cell attachment when unmodified. Gradients of hydroxyapatite or proteins might improve the cellular response to scaffold. Also, we did not investigate the fixation of the implants. Fixation of the 3DP block in bone and the fixation of the ES cuff to tendon will be important to address in future work to further highlight the clinical potential of the biphasic scaffolds. Furthermore, the biocompatibility assays remained very basic. Future biological characterization will require the use of primary cells of the supraspinatus tendon and bone, co-cultures, and next-generation sequencing to assess biological response and repair-potential of the scaffolds. Finally, sterilization of our materials was achieved using ethanol. Methods used in medical device manufacture, such as ethylene oxide sterilization, will need to be investigated at a later stage as these can have critical effects on the implant's biological, mechanical, and degradation properties.

6. Conclusion

3D printing and electrospinning can be combined to produce biphasic implant with a robust soft-hard junction for enthesis repair applications. The thermal properties of the polymers used was important since 3D printing involved high temperatures and this affected the mechanical and morphological properties of the ES fibers. The cuff configuration influenced the failure behavior of the scaffolds as twisted yarns did not adhere to the 3D printed blocks as well as parallel filaments. Up to 270 filaments could be fitted in a footprint area of 50 mm², similar to that of the enthesis of the supraspinatus tendon, allowing us to reach clinically relevant strength. The scaffold components were confirmed to be noncytotoxic and cells were shown to proliferate at their surfaces over a period of 14 days. Although promising, future work will be needed to further assess the potential of these synthetic ES cuff – 3DP block biomaterials including investigating more design parameters (chemical and mechanical gradients, cuff configuration, implant geometry, etc.) and utilizing further characterization methods (mechanical and biological).

Appendix A:

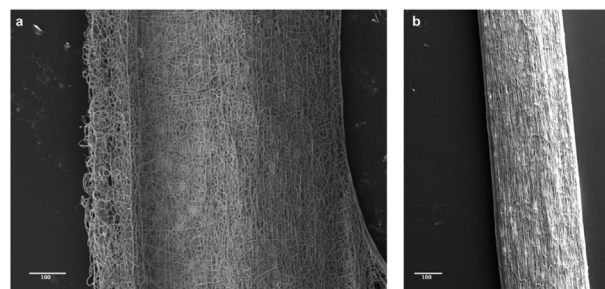


Figure A1. A single unstretched (a) and stretched (b) polydioxanone (PDO) filament image at a magnification of 250x. The scale bar is set at 100 μ m.

Appendix B: Thermal Analysis

The thermographs of DSC for the PDO and PCL samples heated at different temperatures compared to RT are shown in Figure B1. The graphs show the heat flow associated with the transitions of the polymer as a function of time and temperature and have a few identifiable regions. The main melting peak of PDO is around 106 °C and is similarly shaped for most samples (Figure B1A). Small endothermic peaks can be observed around 40 °C, corresponding to an annealing peak with a shift in temperature. A clear exothermic peak is observed around 80 °C just before the melting peak for samples heated at 100 °C, 110 °C, and 120 °C, indicating recrystallization of the samples. For the PCL samples, no annealing or recrystallization peaks are present (Figure B1B). The main melting peak is around 58 °C and shows a difference in the narrowness and elongation of the peaks for all samples with an onset of melting around 30 °C. There is a trend of a broader and shorter peak for samples heated at increasing temperatures, with the broadest and shortest peak for samples heated at 120 °C. Table B1 shows the calculated heat of fusion and corresponding crystallinity for PDO and PCL, as compared to the values of a 100% crystalline sample, as well as onset of melting, melting point, and relevant heat enthalpies. Crystallinity decreases for PDO samples initially, but peaks for samples heated at 90 °C ($p = 0.0042$), followed by a significant dip at 100 °C ($p = 0.0006$) and a consistently lower value for 110 °C and 120 °C ($p = 0.0114$ and 0.0057 , respectively). Onset of melting seems to be at slightly higher temperatures with increasing treatment temperature, but it decreases for samples heated at 100 °C and over. For the PCL samples, crystallinity is lower for all samples compared to RT and there is a shift in onset of melting as well to a slightly higher temperature, although not significantly. (Figure B2)

PDO and PCL are both a semi-crystalline polymer, meaning that they consist of an amorphous and crystalline region, have a highly ordered molecular structure and exhibit a sharp melting point when exposed to heat.^[87] Higher crystallinity increases the intermolecular bonding resulting in higher strength.^[88] Although the calculated heat of fusion and crystallinity is decreased for both polymer samples as they are heated at higher temperatures (Table B1), it only translates in a significant loss of mechanical properties for the PCL samples. This can be explained by the differences in melting temperature, as the range of temperatures used in this experiment exceeded the melting point of PCL (≈ 58 °C), but only noticeably altered PDO samples around its own melting point (≈ 106 °C). However, heat treatment (annealing) can improve the mechanical properties of polymers because it influences the proportion and organization of amorphous and crystalline regions resulting in an increase in crystallinity. It has been shown previously that mechanical properties of electrospun PDO change marginally when exposed to heat for longer periods^[39] and this might explain why these filaments are also only marginally affected by the printing process. During a heating and cooling cycle, crystallization events can occur before the melting point as polymer chains become more mobile during the heating cycle and give off energy (i.e., heat) when moving into a more stable phase. This is referred to as recrystallization or cold

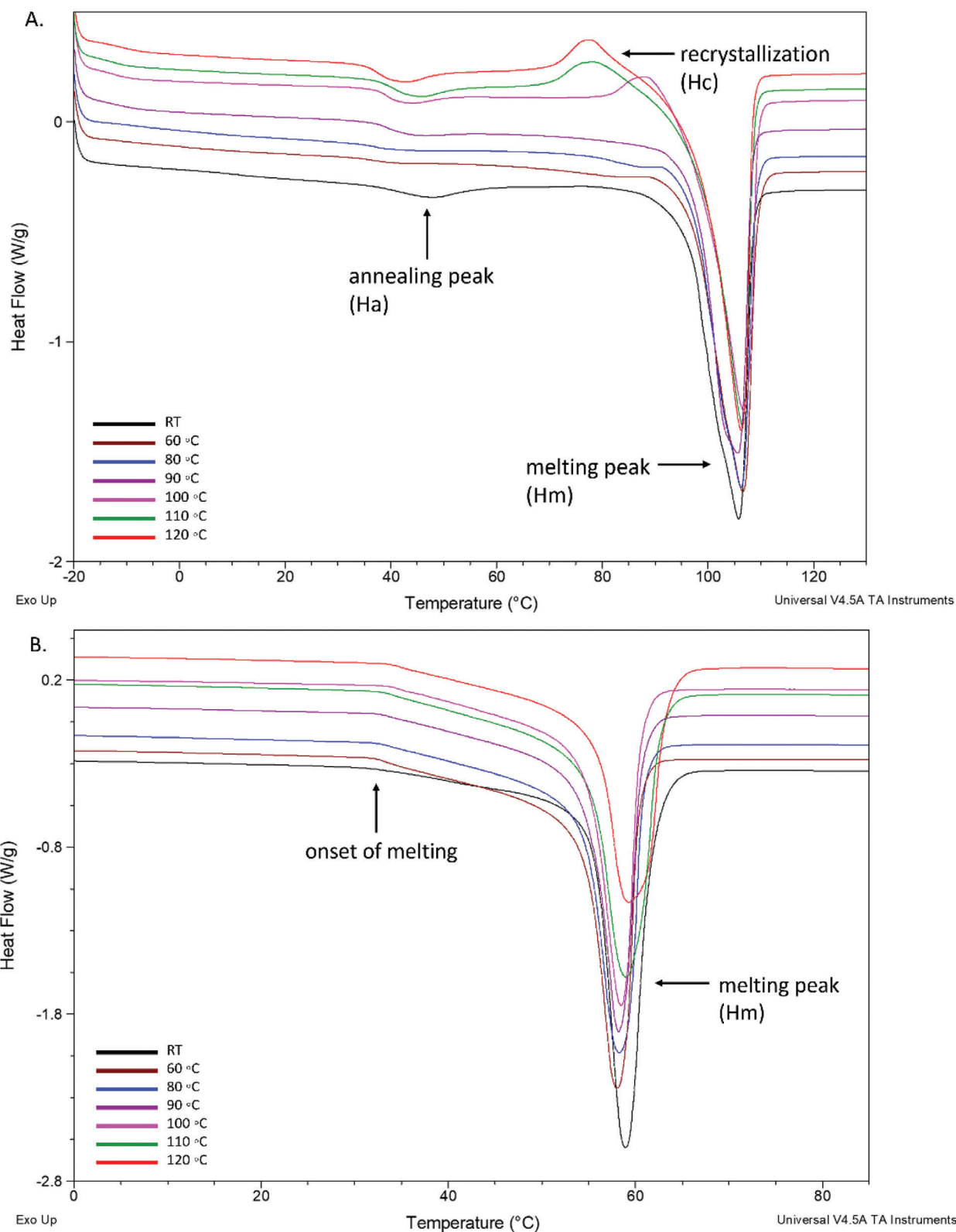


Figure B1. Differential scanning calorimetry (DSC) thermographs for polydioxanone (PDO) samples (A) and polycaprolactone (PCL) samples (B) at room temperature (RT) and heated at temperatures ranging from 60 °C to 120 °C for 1 min. Small endothermic peaks are seen around 40 °C for PDO. The samples heated at 100 °C, 110 °C, and 120 °C show a clear exothermic peak just before the melting peak indicating cold crystallinity. No annealing or crystallinity peaks are present for the PCL samples. All samples have a similar onset of melting but differ in the elongation and narrowness of their respective melting peaks, $n = 3$.

Table B1. Thermal properties of polydioxanone (PDO) filaments subjected to high temperatures (ranging from 60 °C to 120 °C) for 1 min.

	Treatment	T_m [°C]	$T_{m, onset}$ [°C]	ΔH_m [J g ⁻¹]	T_c [°C]	ΔH_c [J g ⁻¹]	T_a [°C]	ΔH_a [J g ⁻¹]	ΔH_{total} [J g ⁻¹]	Crystallinity [%] (<i>p</i> -value)
PDO cuff	RT control	105.8 ± 0.1	87.8 ± 0.7	74.2 ± 2.2	—	—	47.2 ± 0.7	3.8 ± 0.9	78.0 ± 2.1	55.2 ± 1.5
	60 °C	106.3 ± 0.3	89.1 ± 1.3	77.3 ± 2.2	—	—	—	—	77.3 ± 2.2	54.8 ± 1.6 (0.9998)
	80 °C	106.1 ± 0.2	91.8 ± 0.9	77.2 ± 0.9	—	—	—	—	77.2 ± 0.9	54.7 ± 0.6 (0.9996)
	90 °C	105.9 ± 0.3	92.0 ± 0.6	85.0 ± 2.3	—	—	43.3 ± 1.0	1.7 ± 0.4	86.7 ± 2.3	61.4 ± 1.7 (0.0042)
	100 °C	106.7 ± 0.1	90.8 ± 1.1	68.7 ± 1.1	89.4 ± 1.4	3.4 ± 1.7	41.0 ± 0.9	2.0 ± 0.5	67.2 ± 2.3	47.6 ± 1.6 (0.0006)
	110 °C	106.6 ± 0.2	83.1 ± 1.4	74.9 ± 4.3	80.0 ± 2.8	8.5 ± 1.3	43.7 ± 0.8	3.8 ± 0.4	70.3 ± 3.5	49.8 ± 2.5 (0.0114)
	120 °C	106.4 ± 0.3	79.8 ± 1.7	73.9 ± 1.6	77.9 ± 0.2	8.3 ± 0.4	41.1 ± 0.5	3.9 ± 0.3	69.6 ± 1.4	49.3 ± 1.0 (0.0057)
PCL cuff	RT control	56.8 ± 0.2	30.7 ± 0.9	79.3 ± 0.2	—	—	—	—	80.1 ± 2.1	57.5 ± 1.5
	60 °C	53.6 ± 0.7	32.0 ± 0.1	74.9 ± 0.9	—	—	—	—	73.6 ± 1.8	52.7 ± 1.3 (0.1669)
	80 °C	53.1 ± 0.7	32.2 ± 0.3	74.7 ± 1.0	—	—	—	—	73.9 ± 2.3	52.9 ± 1.7 (0.1372)
	90 °C	53.5 ± 0.5	33.0 ± 0.6	74.7 ± 0.7	—	—	—	—	72.6 ± 1.1	52.0 ± 0.8 (0.1409)
	100 °C	52.1 ± 1.7	33.9 ± 0.8	72.7 ± 2.3	—	—	—	—	71.6 ± 3.5	51.3 ± 2.5 (0.0153)
	110 °C	53.9 ± 2.9	33.3 ± 0.4	75.2 ± 4.1	—	—	—	—	75.2 ± 4.1	53.9 ± 2.9 (0.2298)
	120 °C	52.4 ± 1.3	33.9 ± 0.5	73.2 ± 1.8	—	—	—	—	70.2 ± 2.9	50.3 ± 2.1 (0.0265)

- *p*-values refer to RT control values.

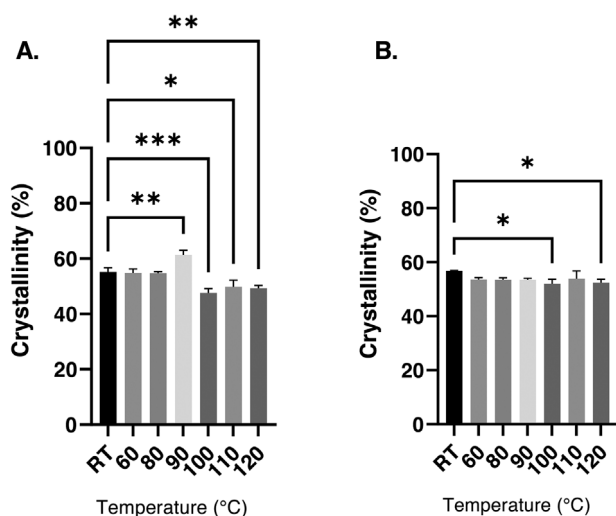


Figure B2. Crystallinity values for polydioxanone (PDO) (A) and polycaprolactone (PCL) (B). Values of *p* < 0.05 are considered significant.

crystallization and can be observed in the PDO thermograms around 80 °C, just before the melting peak. It only occurs for samples that were pre-heated at 100 °C, 110 °C, and 120 °C and has been previously observed in PDO and PLLA samples that were subject to annealing.^[41,89] The small endothermic peaks around 40 °C are annealing peaks and give information about the previous heat history of the sample.^[90] The location of the peaks depends on the annealing temperature and time^[91] and has been reported in semicrystalline polymers undergoing annealing as well.^[39,40] This peak in the samples indicates the formation of crystals that partially melt and recrystallize during the heating cycle until they're completely molten in the main melting peak observed.^[92,93] In the second heating and cooling cycle, after the thermal history has been erased, this peak disappears, as well as the recrystallization peak and all samples show the same single melting peak. For all PCL samples there is an absence of any other endo- or exothermic peaks, bar the melting peak, which could be explained by the fact that the temperatures used to heat the samples were above the melting point of PCL and thermal degradation could therefore not be captured by the DSC experiment, i.e., the samples were already

fully molten before being analyzed by DSC. It could also mean that the time exposed to the heat was not long enough to capture any significant events.^[92]

Acknowledgements

The authors are grateful to 3D LifePrints for their help and expertise in using 3D printing to create the scaffolds. The authors would also like to express the gratitude to the "Patch team" for providing the electrospun filaments and Mr James Fisk at the Institute of Biomedical Engineering (IBME), Oxford for his help in creating the aluminium U-frames. This work was funded by the Interreg 2 Seas programme 2014-2020 3DMed, the Lord Nuffield Trust, and the NIHR Oxford Biomedical Research Centre.

Conflict of Interest

The authors declare no conflict of interest.

Data Availability Statement

The data that support the findings of this study are available from the corresponding author upon reasonable request.

Keywords

3D printing, electrospinning, polycaprolactone, polydioxanone, soft-hard biphasic implant, tendon repair

Received: April 27, 2022
Revised: August 14, 2022
Published online: September 26, 2022

[1] K. Yamaguchi, K. Ditsios, W. D. Middleton, C. F. Hildebolt, L. M. Galatz, S. A. Teefey, *J. Bone Jt. Surg., Am. Vol.* **2006**, *88*, 1699.

- [2] A. J. Carr, C. D. Cooper, M. K. Campbell, J. L. Rees, J. Moser, D. J. Beard, R. Fitzpatrick, A. Gray, J. Dawson, J. Murphy, H. Bruhn, D. Cooper, C. R. Ramsay, *Health Technol. Assess.* **2015**, <https://doi.org/10.3310/hta19800>.
- [3] V. N. Gibbs, P. Raval, J. L. Rees, S. E. Gwilym, *Orthop. Trauma* **2018**, *32*, 165.
- [4] C. A. Cummins, G. A. C. Murrell, *J. Shoulder Elbow Surg.* **2003**, *12*, 128.
- [5] L. S. Oh, B. R. Wolf, M. P. Hall, B. A. Levy, R. G. Marx, *Clin. Orthop. Relat. Res.* **2007**, *455*, 52.
- [6] J. Apostolakis, T. J. S. Durant, C. R. Dwyer, R. P. Russell, J. H. Weinreb, F. Alaei, K. Beitzel, M. B. McCarthy, M. P. Cote, A. D. Mazzocca, *Muscles Ligaments Tendons J.* **2014**, *04*, 333.
- [7] F. A. Barber, M. A. Herbert, R. C. Beavis, F. Barrera Oro, *Arthroscopy* **2008**, *24*, 859.
- [8] F. A. Barber, W. D. Dockery, C. H. Cowden, *Arthroscopy* **2013**, *29*, 1834.
- [9] S. Chaudhry, K. Dehne, F. Hussain, *Orthop. Trauma* **2017**, <https://doi.org/10.1016/j.mporth.2016.12.001>.
- [10] H. Van Der Bracht, T. Van Den Langenbergh, M. Pouillon, S. Verhaselt, P. Verniers, D. Stoffelen, *J. Shoulder Elbow Surg.* **2018**, *27*, 2006.
- [11] F. A. Barber, M. A. Herbert, *Arthroscopy* **2013**, *29*, 832.
- [12] J. Z. Paxton, K. Baar, L. M. Grover, *Orthop. Muscular Sys.* **2013**, <https://doi.org/10.4172/2161-0533.S1-003>.
- [13] A. J. Boys, M. C. Mccorrey, S. Rodeo, L. J. Bonassar, L. A. Estroff, *MRS Commun.* **2017**, *7*, 289.
- [14] R. C. Locke, A. C. Abraham, M. L. Killian, *ACS Biomater. Sci. Eng.* **2017**, *3*, 2633.
- [15] P.-A. Mouthuy, N. Zargar, O. Hakimi, E. Lostis, A. Carr, *Biofabrication* **2015**, *7*, 025006.
- [16] T. Guo, J. Lembong, L. G. Zhang, J. P. Fisher, *Tissue Eng., Part B* **2017**, *23*, 225.
- [17] R. Abhari, A. Carr, P. A. Mouthuy, *Electrofluidodynamic Technologies (EFDTs) for Biomaterials and Medical Devices: Principles and Advances*, Woodhead Publishing, Oxford 2018.
- [18] N. Narayanan, L. Kuang, M. Del Ponte, C. Chain, M. Deng, in *Nanocomposites for Musculoskeletal Tissue Regeneration* (Ed: H. Liu), Woodhead Publishing, Oxford **2016**, p. 3.
- [19] J. A. Martins, A. A. Lach, H. L. Morris, A. J. Carr, P.-A. Mouthuy, *J. Biomater. Appl.* **2019**, *34*, 902.
- [20] R. Dwivedi, S. Kumar, R. Pandey, A. Mahajan, D. Nandana, D. S. Katti, D. Mehrotra, *J. Oral Biol. Craniofacial Res.* **2020**, *10*, 381.
- [21] S. Font Tellado, W. Bonani, E. R. Balmayor, P. Foehr, A. Motta, C. Migliaresi, M. Van Griensven, *Tissue Eng., Part A* **2017**, *23*, 859.
- [22] S.-J. Lee, M. Nowicki, B. Harris, L. G. Zhang, *Tissue Eng., Part A* **2017**, *23*, 491.
- [23] B. Huang, E. Aslan, Z. Jiang, E. Daskalakis, M. Jiao, A. Aldalbahi, C. Vyas, P. Bartolo, *Addit. Manuf.* **2020**, *36*, 101452.
- [24] M. Rampichová, E. Košťáková Kuželová, E. Filová, J. Chvojka, J. Šafka, M. Pelcl, J. Daňková, E. Prosecká, M. Buzgo, M. Plencner, D. Lukáš, E. Amler, *Cell Adhes. Migr.* **2018**, *12*, 271.
- [25] N. W. Pensa, A. S. Curry, P. P. Bonvallet, N. F. Bellis, K. M. Rettig, M. S. Reddy, A. W. Eberhardt, S. L. Bellis, *Biomater. Res.* **2019**, *23*, 22.
- [26] M. Rampichová, E. Košťáková Kuželová, E. Filová, J. Chvojka, J. Šafka, M. Pelcl, J. Daňková, E. Prosecká, M. Buzgo, M. Plencner, D. Lukáš, E. Amler, *Cell Adhes. Migr.* **2018**, *12*, 271.
- [27] C. Vyas, G. Ates, E. Aslan, J. Hart, B. Huang, P. Bartolo, *3D Print. Addit. Manuf.* **2020**, *7*, 105.
- [28] B. Huang, G. Caetano, C. Vyas, J. Blaker, C. Diver, P. Bartolo, *Materials* **2018**, *11*, 129.
- [29] E. Itoi, L. J. Berglund, J. J. Grabowski, F. M. Schultz, E. S. Grownay, B. F. Morrey, K.-N. An, *J. Orthop. Res.* **1995**, *13*, 578.
- [30] E. Itoi, H. C. Hsu, S. W. Carmichael, B. F. Morrey, K. N. An, *J. Anat.* **1995**, *186*, 429.
- [31] T. Matsushashi, A. W. Hooke, K. D. Zhao, A. Goto, J. W. Sperling, S. P. Steinmann, K.-N. An, *Clin. Anat.* **2014**, *27*, 702.
- [32] M. Rickert, H. Georgousis, U. Witzel, *Unfallchir.* **1998**, *101*, 265.
- [33] R. D. J. Smith, N. Zargar, C. P. Brown, N. S. Nagra, S. G. Dakin, S. J. B. Snelling, O. Hakimi, A. Carr, *J. Shoulder Elbow Surg.* **2017**, *26*, 2038.
- [34] T. U. Rashid, R. E. Gorga, W. E. Krause, *Adv. Eng. Mater.* **2021**, *23*, 2100153.
- [35] A. A. Lach, H. L. Morris, J. A. Martins, E. T. Stace, A. J. Carr, P.-A. Mouthuy, *PLoS One* **2019**, *14*, e0214419.
- [36] L. Savić, E. M. Augustyniak, A. Kastensson, S. Snelling, R. E. Abhari, M. Baldwin, A. Price, W. Jackson, A. Carr, P.-A. Mouthuy, *Mater. Sci. Eng., C* **2021**, *129*, 112414.
- [37] H. Maleki, H. Barani, *Polym. Eng. Sci.* **2018**, *58*, 1091.
- [38] R. E. Abhari, P. A. Mouthuy, A. Vernet, J. E. Schneider, C. P. Brown, A. J. Carr, *Polym. Test.* **2018**, *69*, 188.
- [39] R. E. Abhari, P.-A. Mouthuy, N. Zargar, C. Brown, A. Carr, *J. Mech. Behav. Biomed. Mater.* **2017**, *67*, 127.
- [40] S. Tan, A. Su, W. Li, E. Zhou, *J. Polym. Sci., Part B: Polym. Phys.* **2000**, *38*, 53.
- [41] E. Lizundia, S. Petisco, J.-R. Sarasua, *J. Mech. Behav. Biomed. Mater.* **2013**, *17*, 242.
- [42] K. Ishikiriya, M. Pyda, G. Zhang, T. Forschner, J. Grebowicz, B. Wunderlich, *J. Macromol. Sci., Part B: Phys.* **1998**, *37*, 27.
- [43] R. Smith, A. Carr, S. Dakin, S. Snelling, C. Yapp, O. Hakimi, *Eur. Cells Mater.* **2016**, *31*, 107.
- [44] I. S. O., *ISO 10993-5:2009*, **2009**, <https://www.iso.org/standard/36406.html>
- [45] H. K. Selle, B. Bar-On, G. Marom, H. Daniel Wagner, *Mater. Sci. Eng., C* **2015**, <https://doi.org/10.1016/j.msec.2014.11.001>
- [46] N. Pan, D. Brookstein, *J. Appl. Polym. Sci.* **2002**, *83*, 610.
- [47] D. U. Shah, P. J. Schubel, M. J. Clifford, *J. Compos. Mater.* **2012**, *47*, 425.
- [48] A. A. Conte, K. Sun, X. Hu, V. Z. Beachley, *Front. Chem.* **2020**, *8*, 610.
- [49] O. S. Manoukian, M. R. Arul, N. Sardashti, T. Stedman, R. James, S. Rudraiah, S. G. Kumbar, *J. Appl. Polym. Sci.* **2018**, *135*, 46068.
- [50] L. Liverani, A. Boccacini, *Nanomaterials* **2016**, *6*, 75.
- [51] A. Salerno, D. Guarnieri, M. Iannone, S. Zepetelli, P. A. Netti, *Tissue Eng., Part A* **2010**, *16*, 2661.
- [52] J. Xue, T. Wu, Y. Dai, Y. Xia, *Chem. Rev.* **2019**, *119*, 5298.
- [53] F. Qu, F. Guilak, R. L. Mauck, *Nat. Rev. Rheumatol.* **2019**, *15*, 167.
- [54] M. Rashid, J. Dudhia, S. G. Dakin, S. Snelling, A. Lach, R. De Godoy, P.-A. Mouthuy, R. Smith, M. Morrey, A. J. Carr, *PLoS One* **2020**, *15*, e0234982.
- [55] R. E. Abhari, A. J. Carr, P.-A. Mouthuy, in *Electrofluidodynamic Technologies (EFDTs) for Biomaterials and Medical Devices* (Eds: V. Guarino, L. Ambrosio), Woodhead Publishing, Cambridge, England **2018**, p. 295.
- [56] A. Nezhentsev, R. E. Abhari, M. J. Baldwin, J. Y. Mimpfen, E. Augustyniak, M. Isaacs, P. A. Mouthuy, A. J. Carr, S. J. B. Snelling, *Transl. Sports Med.* **2021**, *4*, 409.
- [57] S. R. Caliri, D. W. Weisgerber, W. K. Grier, Z. Mahmassani, M. D. Boppart, B. A. C. Harley, *Adv. Healthcare Mater.* **2015**, *4*, 831.
- [58] S. Samavedi, P. Vaidya, P. Gaddam, A. R. Whittington, A. S. Goldstein, *Biotechnol. Bioeng.* **2014**, *111*, 2549.
- [59] J. Xie, X. Li, J. Lipner, C. N. Manning, A. G. Schwartz, S. Thomopoulos, Y. Xia, *Nanoscale* **2010**, *2*, 923.
- [60] M. Ramalingam, M. F. Young, V. Thomas, L. Sun, L. C. Chow, C. K. Tison, K. Chatterjee, W. C. Miles, C. G. Simon, *J. Biomater. Appl.* **2013**, *27*, 695.
- [61] C. Erksen, D. M. Kalyon, H. Wang, *Biomaterials* **2008**, *29*, 4065.
- [62] X. Li, J. Xie, J. Lipner, X. Yuan, S. Thomopoulos, Y. Xia, *Nano Lett.* **2009**, *9*, 2763.
- [63] I. Calejo, R. Costa-Almeida, R. L. Reis, M. E. Gomes, *Tissue Eng., Part B* **2019**, *25*, 330.

- [64] Y. Cao, S. Yang, D. Zhao, Y. Li, S. S. Cheong, D. Han, Q. Li, *J. Orthop. Transl.* **2020**, *23*, 89.
- [65] C. R. Correia, R. L. Reis, J. F. Mano, *Adv. Exp. Med. Biol.* **2015**, *881*, 143.
- [66] A. Islam, M. S. Bohl, A. G. Tsai, M. Younesi, R. Gillespie, O. Akkus, *Clin. Biomech.* **2015**, *30*, 669.
- [67] B. B. Rothrauff, T. Pauyo, R. E. Debski, M. W. Rodosky, R. S. Tuan, V. Musahl, *Tissue Eng., Part B* **2017**, *23*, 318.
- [68] C. M. Jobe, J. P. Lannotti, *J. Shoulder Elbow Surg.* **1995**, *4*, 281.
- [69] S.-J. Lee, M. Nowicki, B. Harris, L. G. Zhang, *Tissue Eng., Part A* **2017**, *23*, 491.
- [70] L. F. Mellor, P. Huebner, S. Cai, M. Mohiti-Asli, M. A. Taylor, J. Spang, R. A. Shirwaiker, E. G. Lobo, *Biomed Res. Int.* **2017**, *2017*, 6956794.
- [71] Y. Yu, S. Hua, M. Yang, Z. Fu, S. Teng, K. Niu, Q. Zhao, C. Yi, *RSC Adv.* **2016**, *6*, 110557.
- [72] T. Mochizuki, H. Sugaya, M. Uomizu, K. Maeda, K. Matsuki, I. Sekiya, T. Muneta, K. Akita, *J. Bone Jt. Surg., Am. Vol.* **2009**, <https://doi.org/10.2106/JBJS.H.01426>
- [73] B. M. Berghs, T. Derveaux, W. Speeckaert, K. Vanslambrouck, L. F. De Wilde, *J. Shoulder Elbow Surg.* **2011**, *20*, 637.
- [74] A. D. Mazzocca, P. J. Millett, C. A. Guanche, S. A. Santangelo, R. A. Arciero, *Am. J. Sports Med.* **2005**, *33*, 1861.
- [75] C. Gerber, B. Fuchs, J. Hodler, *J. Bone Jt. Surg., Am. Vol.* **2000**, *82*, 505.
- [76] W. Z. Burkhead, J. G. Skedros, P. J. O'rourke, W. A. Pierce, T. C. Pitts, *Clin. Orthop. Relat. Res.* **2007**, *461*, 106.
- [77] A. F. C. Aristizabal, F. A. Barber, *Ann. Jt.* **2021**, *6*, 18.
- [78] A. Inoue, E. Chosa, K. Goto, N. Tajima, *Knee Surg. Sports Traumatol. Arthrosc.* **2013**, *21*, 1151.
- [79] C.-Y. Huang, V. M. Wang, R. J. Pawluk, J. S. Bucchieri, W. N. Levine, L. U. Bigliani, V. C. Mow, E. L. Flatow, *J. Orthop. Res.* **2005**, *23*, 924.
- [80] T. Nakajima, N. Rokuuma, K. Hamada, T. Tomatsu, H. Fukuda, *J. Shoulder Elbow Surg.* **1994**, *3*, 79.
- [81] M. J. Bey, H. K. Song, F. W. Wehrli, L. J. Soslowsky, *J. Orthop. Res.* **2002**, *20*, 869.
- [82] H. Ramakrishna, T. Li, T. He, J. Temple, M. W. King, A. Spagnoli, *Biomater. Res.* **2019**, *23*, 11.
- [83] Y. Jiao, C. Li, L. Liu, F. Wang, X. Liu, J. Mao, L. u Wang, *Biomater. Sci.* **2020**, *8*, 3574.
- [84] A. Sensini, L. Cristofolini, *Materials* **2018**, *11*, 1963.
- [85] R. L. Waltrip, N. Zheng, J. R. Dugas, J. R. Andrews, *The Am. J. Sports Med.* **2003**, *31*, 493.
- [86] S. S. Burkhart, J. L. Diaz Pagã N, M. A. Wirth, K. A. Athanasiou, *Arthroscopy* **1997**, *13*, 720.
- [87] N. Goonoo, R. Jeetah, A. Bhaw-Luximon, D. Jhurry, *Eur. J. Pharm. Biopharm.* **2015**, *97*, 371.
- [88] K. Balani, *Biosurfaces: A Materials Science and Engineering Perspective*, ACerS–Wiley, Hoboken, NJ **2014**.
- [89] W. Zhang, I. Ullah, L. Shi, Y. Zhang, H. Ou, J. Zhou, M. W. Ullah, X. Zhang, W. Li, *Mater. Des.* **2019**, *180*, 107946.
- [90] D. J. Burlett, in *Handbook of Thermal Analysis and Calorimetry*, (Eds: M. E. Brown, P. K. Gallagher), Vol. 5, Elsevier Science B.V, Oxford **2008**, p. 695.
- [91] M. Bonnet, K.-D. Rogausch, J. Petermann, *Colloid Polym. Sci.* **1999**, *277*, 513.
- [92] T. Mukhametzyanov, J. W. P. Schmelzer, E. Yarko, A. Abdullin, M. Ziganshin, I. Sedov, C. Schick, *Polymers* **2021**, *13*, 3617.
- [93] M. A. Sabino, J. L. Feijoo, A. J. Müller, *Macromol. Chem. Phys.* **2000**, *201*, 2687.